INTERNATIONAL JOURNAL FOR NUMERICAL AND ANALYTICAL METHODS IN GEOMECHANICS
Int. J. Numer. Anal. Meth. Geomech. 2010; **34**:821–837
Published online 24 September 2009 in Wiley InterScience (www.interscience.wiley.com). DOI: 10.1002/nag.835

Flat boundaries and their effect on sand testing

G. Marketos[1,2,*,†] and Malcolm D. Bolton[2]

[1]*Currently part of the Geology and Geophysics Group, National Oceanography Centre, Southampton, U.K.*
[2]*Geotechnical and Environmental Engineering Research Group, Engineering Department, University of Cambridge, U.K.*

SUMMARY

A study of the effect of the use of flat boundaries on the stressing of a sample of an idealized granular material with no applied shear is presented. Discrete element method (DEM) data of 1D compression were analysed and the local strain field inside the sample was investigated as the sample was stressed. A best-fit strain was seen to best describe the material behaviour free from boundary effects. The individual particle displacements were probed, providing insight into the behaviour of particles adjacent to the boundaries. In addition, the porosity and force distribution inside the sample were observed, allowing for estimates of the width of a boundary region to be made. This region, non-representative of far-field material behaviour, will affect the behaviour of a granular sample in DEM or laboratory tests, with local porosity differences leading to a change in the transport properties of the sample, and force distribution changes leading to a bias in the location of grain cracking or crushing events for sufficiently high stress levels. Nevertheless, the largest effect of the boundary region was a severe underestimation of the stiffness of a granular material.

Received 28 October 2008; Revised 21 July 2009; Accepted 21 July 2009

KEY WORDS: boundary effects; discrete element model; 1D compression; strain; sand; micromechanics

INTRODUCTION

Laboratory testing of samples of granular materials is often performed with the purpose of finding representative material properties. Practicalities usually dictate the use of rigid surfaces, especially for the top and bottom boundaries of the sample, perhaps with flexible boundaries at the sides as with triaxial tests. Sand-boundary contacts are also encountered in a number of other common civil engineering applications (see Figure 1 for some examples) and in the majority of discrete element method (DEM) simulations of granular materials.

*Correspondence to: G. Marketos, Currently part of the Geology and Geophysics group, National Oceanography Centre, European Way, Southampton, SO14 3ZH, U.K.
†E-mail: giorgosmarketos@yahoo.com

Contract/grant sponsor: A. S. Onassis and the A. G. Leventis Foundations

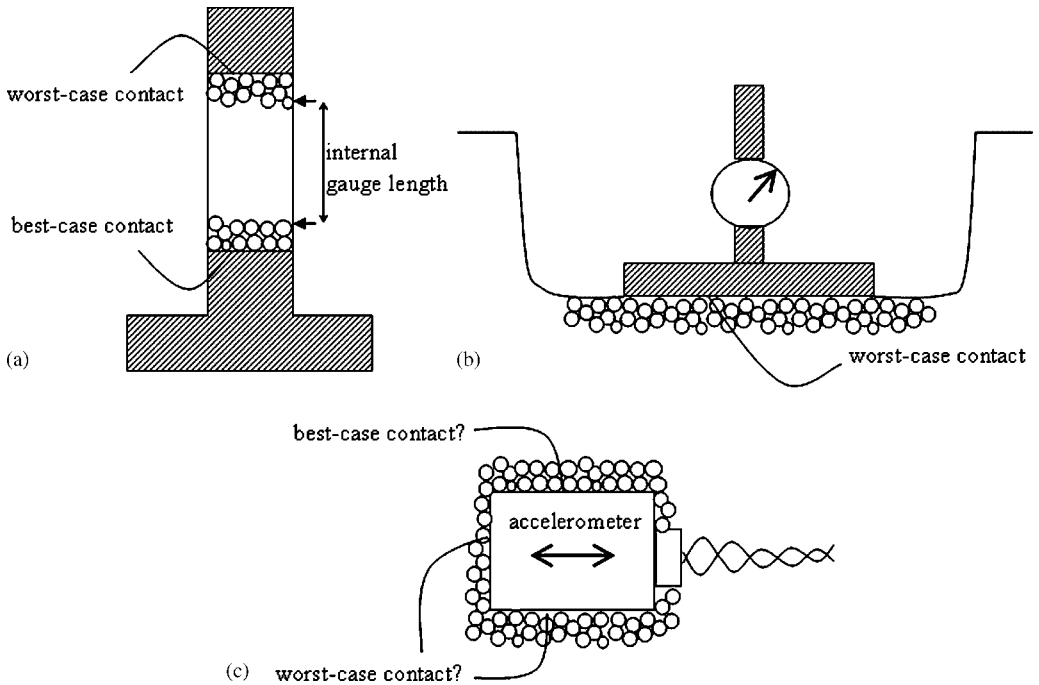

Figure 1. Influence of solid-grain interfaces: some applications.

The use of flat rigid boundaries will disrupt the grain packing to an extent that might depend, among others, on the method of sample preparation. The boundary-particle interface may influence the fabric and voids ratio of the material in contact. A particular problem concerns the bedding error induced when a top platen is placed over a sample that is inevitably irregular at the granular scale. This can have a non-negligible effect on the local strain measured there, in some cases leading to total strain measurements for the sample not representative of mass soil behaviour. A solution to this in laboratory element testing is the use of internal strain measurements sufficiently far from the boundary region (e.g. [1], see Figure 1(a)).

However, the extent of the non-representative boundary region above and below a granular sample has not been clearly defined. There is even less guidance on the implications of boundary effects in physical model tests such as oedometer tests or small-scale field tests such as plate bearing tests (see Figure 1(b)), in which internal strain measurements are not possible, or the coupling and response of buried instruments such as accelerometers (see Figure 1(c)). It is often assumed that boundary effects in sand samples are negligible provided that the sample size to particle size ratio is sufficiently large. Head [2] suggests a minimum value for the ratio of sample dimension to maximum particle diameter for standard tests ranging from 5 for compressive strength and consolidation tests to 10 for shearbox and 12 for permeability tests.

Previous studies on boundary effects have considered only the density ([3–6]) and coordination number variations produced near a rigid surface (e.g. [7]) for samples at their unstressed state. Hardin [3] showed that a flat boundary will induce a local density decrease due to lack of fit between the surface and spherical particles. Hardin's study assumed that particles will form crystal

DOI: 10.1002/nag

structures, for which analytical solutions could be developed. However, grain crystal packing does not occur in polysized mixtures in nature. Chan and Ng [6] investigated local porosity fluctuations near a flat boundary for a more random simulated granular pack; their study is interesting but the boundary effect seems to be masked by the large porosity fluctuations, the origin of which is unclear. We have therefore revisited here the effect of a flat boundary on the vertical spatial distribution of porosity inside a granular sample.

Roblee *et al.* [4] and Reyes and Iglesia [5] found that the porosity was affected in a region extending three grain diameters from a curved cylindrical wall in packs of monosized spheres. The results of Roblee *et al.* [4] indicate that grain shape has a significant effect on the width of the boundary region, while Reyes and Iglesia's [5] results suggest that the width of the boundary region decreases as the grain size distribution is broadened. One should note, however, that the important effects of grain size distribution and grain shape on the extent of the boundary regions will not be investigated here. The current study will focus on an assembly of spheres with a maximum to minimum grain size ratio of 2, similar to sands commonly used in the laboratory.

The effect on density variations of stressing such an assembly has not been studied in the past. Another aspect of behaviour that has eluded investigation until now is the effect of a rigid boundary on the force propagation through a sample. It is therefore necessary to quantify the influence of a boundary in the current more realistic randomly packed assembly of grains, and to investigate local force/stress variations. This could help to fully understand and mitigate boundary effects in sand testing.

For this reason an investigation was conducted based on data from DEM simulations of a polysized mixture of spherical particles confined by flat, rigid surfaces. This provided data on the positions of particles and distributions of contact forces that would otherwise be impossible to obtain. Data of particle positions and displacements were used to investigate the local distribution of strain inside a sample in comparison with the strain calculated at the boundaries. Furthermore, data of positions and force magnitudes were treated using statistical arguments in order to obtain mean values for the more representative middle region, and to identify the extent of the boundary region based on deviations from the mean. This investigation of boundary effects will also contribute to assess the feasibility of using DEM to solve boundary value problems such as foundations in sand.

One should note that the results from the 1D compression tests presented here are only strictly applicable to cases where the boundary applies no shearing to the particles in contact with it, as shearing would modify the local micromechanism of deformation in the boundary region. Nevertheless, the current study should provide invaluable insight to engineers confronted with a soil-boundary problem that involves shearing too.

THE DISCRETE ELEMENT METHOD (DEM)

Three-dimensional computer DEM simulations of the stressing of a sand sample were performed using the commercially available PFC^{3D} software package, based on the initial work of Cundall and Strack [8]. A concise description of the code can be found in the PFC3D manual [9].

The sample used here consisted of 30 892 spherical particles whose radii were uniformly distributed between 1 and 2 mm. This ensured that the ratio of maximum to minimum grain size was 2, as is common in experimental studies. No attempt has been made to study the effect of grain shape on the extent of the region affected by the presence of a flat boundary. Nevertheless,

DOI: 10.1002/nag

this study should provide a good insight into the interface behaviour when the sand grains are sub-rounded. The inter-particle interaction was modelled by linear springs of stiffness 4×10^6 N/m, a local damping coefficient of 0.7 and a frictional coefficient of 0.5. The sample had initial dimensions of $90 \times 90 \times 107$ mm and an initial porosity of 44%, which corresponds to a voids ratio of 0.80, when completely unstressed. It was bounded by frictionless flat walls, also of stiffness 4×10^6 N/m. The selection of DEM parameters is thoroughly discussed in [10].

The sample was generated by numerically simulating the 'dry pluviation' experimental sample preparation technique. This method assumes no momentum exchange between the grain to be placed and the already-placed grains and so is thought to represent very well sedimentation of grains from a low height. Spheres were randomly generated inside a space bounded by five walls in the form of an open cubical box and were then moved vertically downwards one-at-a-time until they were in contact with another sphere already placed. They were then forced to slide on the surfaces of other, already-placed particles, until they reached a stable equilibrium position. This procedure was repeated until the particle column reached a height much larger than the required specimen height. Particles with centroids lying above a specific vertical level were then removed and a flat wall was placed on top, prior to being driven down without rotation, to compress the sample.

This preparation method resulted in a loose, anisotropic grain fabric [10]. One should note that the top and bottom grain-boundary interfaces thus produced were very different from each other. The bottom represented a 'best-case' boundary contact as the grains were sequentially deposited on the flat boundary and so made contact with it at a large number of points. The top grain surface represented a 'worst-case' scenario as it was much more uneven, containing more voids and making contact with the top platen at fewer points. Both surfaces are however very similar to surfaces commonly encountered in a number of common civil engineering applications (see Figure 1).

The 107 mm high DEM sample was then tested under 1D compression in the absence of gravity. Both top and bottom platens were moved inward with the same speed, resulting in a vertical shortening rate of 100 mm/s, giving a compressive strain rate of about $1\,s^{-1}$. The use of a large strain rate is dictated by the need to minimize computation time, and the one used here is rather more conservative than the strain rate of $75\,s^{-1}$ used in DEM simulations by Cheng *et al.* [11]. Moreover, Cheng *et al.* demonstrated that relatively small distortions of stress–strain behaviour were obtained in their analogous DEM simulations even at the much larger strain rate of $150\,s^{-1}$. The effects of strain rate were seen by Marketos [10], not to affect the results qualitatively, but only to introduce small quantitative changes. For the simulations reported here the only micromechanism possible was particle rearrangement, as grain damage was not allowed. Figure 2 contains a plot of the vertical stress versus vertical macro strain inferred from boundary displacements. The distribution of strain inside the sample was then investigated for a number of strain increments throughout the simulation. One should note that the sign convention is compression positive.

STRAIN CALCULATION

One approach to strain calculation for granular samples involves the direct use of the boundary displacement values, as with classical materials. Another approach is to attempt to infer internal strain values, but it is difficult to define and track the movement of a reference plane inside a sample as the particles move erratically across it. Laboratory measurements of internal strain in

DOI: 10.1002/nag

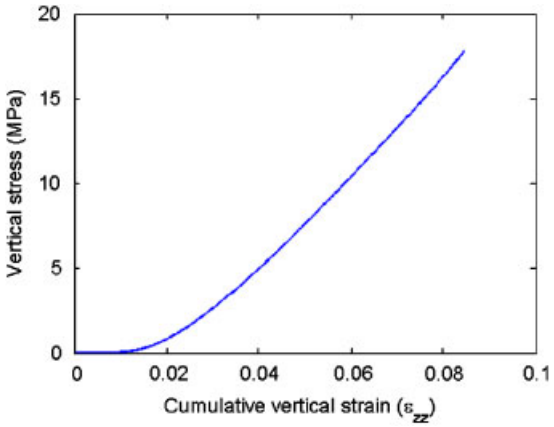

Figure 2. A plot of vertical stress versus cumulative macro vertical strain measured at the sample boundary.

a sample are based on the assumption that the movements recorded at the surface membrane are equal to the movement of such internal planes, thus introducing an uncertainty to the strain calculation.

Unlike common laboratory studies, DEM computer simulations of granular materials and CT scans of tested specimens can output the individual displacements of each particle. A measure of the internal strain can then be obtained by calculating some deformation gradient. A summary of different proposed methods for strain calculation based on individual particle displacements is given by O'Sullivan *et al.* [12] and Bagi [13]. A few key methods will be mentioned here. Bagi [13] and other similar methods (e.g. [14]) require a partition of space in different cells based on the particle centroids. Inside each space cell the deformation gradient is assumed constant and its *volume average* is calculated for the region of interest. These methods have the disadvantage of increased complexity and computation time due to the volumetric partitioning process.

Another approach is the calculation of the *best-fit* strain inside the specified particle region, which is conceptually different from the *volume average* mentioned above. A conceptually similar method was proposed by Cundall and is described in the PFC^{3D} manual [9]. A deformation gradient tensor, α_{ij}, is fitted to the actual particle displacements in the least-squares sense by making use of Equation (1), which is a system of 9 equations with 9 unknowns, the unknowns here being the best-fit deformation gradients $\partial u/\partial x$, $\partial u/\partial y$, $\partial v/\partial x$, etc.

$$\begin{bmatrix} \sum_{i=1}^{N} \Delta u_i (x_i - x_c) & \sum_{i=1}^{N} \Delta u_i (y_i - y_c) & \sum_{i=1}^{N} \Delta u_i (z_i - z_c) \\ \sum_{i=1}^{N} \Delta v_i (x_i - x_c) & \sum_{i=1}^{N} \Delta v_i (y_i - y_c) & \sum_{i=1}^{N} \Delta v_i (z_i - z_c) \\ \sum_{i=1}^{N} \Delta w_i (x_i - x_c) & \sum_{i=1}^{N} \Delta w_i (y_i - y_c) & \sum_{i=1}^{N} \Delta w_i (z_i - z_c) \end{bmatrix} =$$

DOI: 10.1002/nag

$$\begin{bmatrix} \frac{\partial u}{\partial x} & \frac{\partial u}{\partial y} & \frac{\partial u}{\partial z} \\ \frac{\partial v}{\partial x} & \frac{\partial v}{\partial y} & \frac{\partial v}{\partial z} \\ \frac{\partial w}{\partial x} & \frac{\partial w}{\partial y} & \frac{\partial w}{\partial z} \end{bmatrix} \begin{bmatrix} \sum_{i=1}^{N}(x_i-x_c)(x_i-x_c) & \sum_{i=1}^{N}(x_i-x_c)(y_i-y_c) & \sum_{i=1}^{N}(x_i-x_c)(z_i-z_c) \\ \sum_{i=1}^{N}(y_i-y_c)(x_i-x_c) & \sum_{i=1}^{N}(y_i-y_c)(y_i-y_c) & \sum_{i=1}^{N}(y_i-y_c)(z_i-z_c) \\ \sum_{i=1}^{N}(z_i-z_c)(x_i-x_c) & \sum_{i=1}^{N}(z_i-z_c)(y_i-y_c) & \sum_{i=1}^{N}(z_i-z_c)(z_i-z_c) \end{bmatrix} \quad (1)$$

Here Δu, Δv, Δw are the individual particle displacements in the x, y (horizontal) and z (vertical) directions, respectively, the subscript indicates which particle the quantities relate to, and a subscript c indicates the centroid of the volume for which the deformation gradient is calculated, which contains a total of N particles. One notes that Equation (1) contains summations of the products of micromechanical variables that are readily available through DEM.

For this work, the least-squares solution for the deformation gradient tensor was calculated by using the data of particle coordinates at two different stress levels, while the initial configuration was taken as the reference point. The deformation gradient also contains rigid body rotations. If the strain tensor ε_{ij} is required, only the symmetric part of the deformation gradient tensor α_{ij} should be kept (Equation (2)), as the antisymmetric part describes sample rotation.

$$\varepsilon_{ij} = 0.5(\alpha_{ij} + \alpha_{ji}) \quad (2)$$

STRAIN RESULTS

In what follows the specimen was divided into slices that ran the full length of the sample in the horizontal direction and were 1 mean particle diameter (i.e. 3 mm) thick in the vertical (loading) direction. Equation (1) was solved and Equation (2) applied for all grains in each slice to get the local best-fit strain. One should note that the local best-fit strain values so calculated were very similar to local best-fit strain values calculated when excluding grains within two mean grain diameters from the vertical boundaries (see Figure 3 for example). This does not mean that there is no lateral boundary region though; an investigation of the potentially important lateral boundary effect is beyond the scope of this study.

Figure 3 contains a plot of the local best-fit vertical strain versus the distance from the bottom flat boundary for the stress increment from 0 (completely unstressed assembly) to 1 MPa. Figures 4 and 5 are similar plots for the stress increments of 1–6 MPa and 6–12 MPa, respectively. The best-fit vertical strain for the whole sample and the strain as calculated from boundary displacement values were also plotted on each of these figures for comparison. One should recall that only the vertical strain ε_{zz} was applied by the boundaries, consistent with 1D compression in the z-direction. One should further note that in Figure 3 the point for the top slice (35, 0.942) lay out of the plotting range, as the strain value observed there was more than 10 times larger than the rest. This was done to avoid rescaling the plotting window, which would decrease the resolution of the plot, obscuring the behaviour.

One observes in Figures 3–5 that the results for the best-fit internal vertical strain and the external macro strain as calculated using boundary displacement values were not identical. Bagi [13] also observed this effect in 2D simulations of a uniaxial compression test, showing data which

DOI: 10.1002/nag

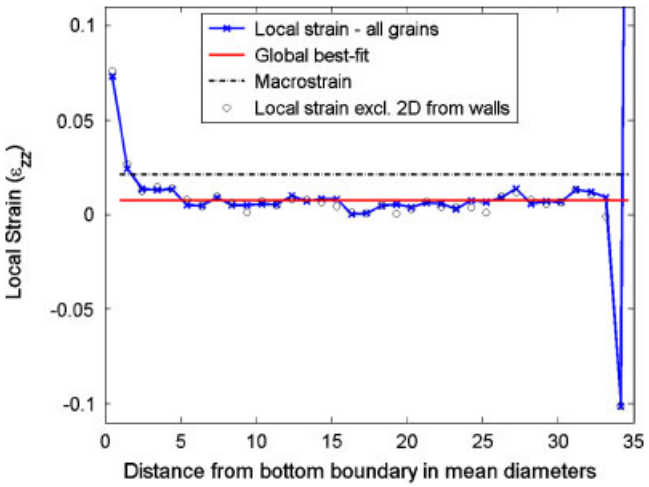

Figure 3. Local best-fit strain versus distance from the bottom boundary non-dimensionalized by the mean particle diameter: stress increment 0–1 MPa. The local best-fit strain as calculated by excluding grains within two mean diameters from the lateral boundaries is also plotted.

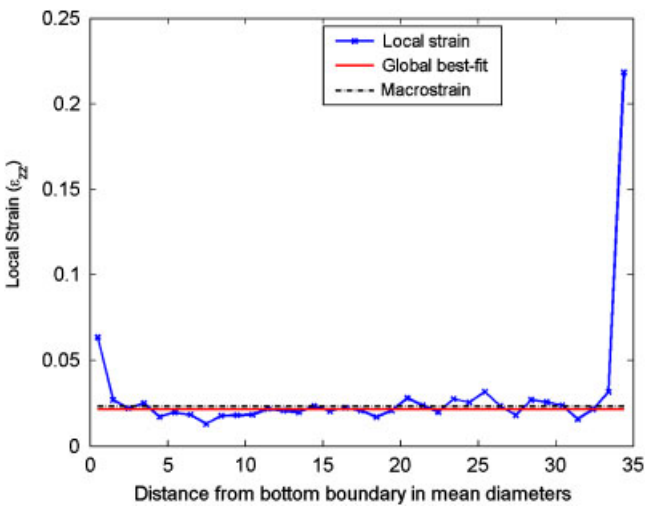

Figure 4. Local best-fit strain versus distance from the bottom boundary non-dimensionalized by the mean particle diameter: stress increment 1–6 MPa.

indicate that the discrepancy decreases with increased straining. This was confirmed here, and an explanation can now be given. Between 0 and 1 MPa, the macro strain was 2.13% while the best-fit strain was 0.72% (a factor 3 error). This error decreased to factor 1.07 between 1 and 6 MPa (a macro strain of 2.29% when the best-fit strain was 2.12%) and then further decreased to factor 0.99 (a macro strain of 2.17% when the best-fit strain was 2.19%) between 6 and 12 MPa.

DOI: 10.1002/nag

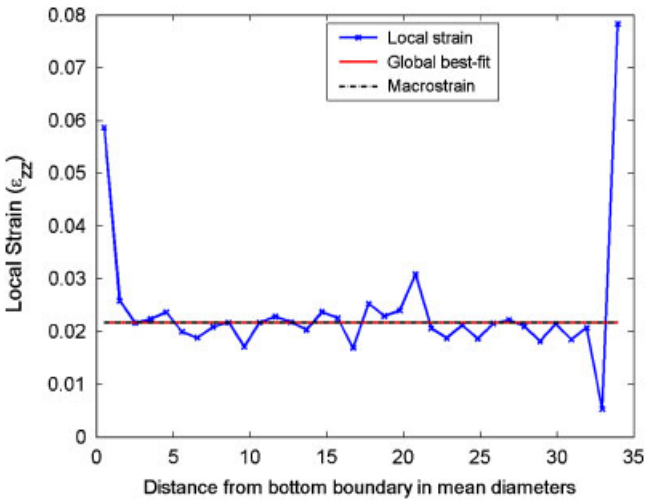

Figure 5. Local best-fit strain versus distance from the bottom boundary non-dimensionalized by the mean particle diameter: stress increment 6–12 MPa.

The error between the vertical best-fit strain and the vertical macro strain was unacceptably large for the initial stage of the deformation (0–1 MPa). One might think that it is the macro strain that gave the correct strain value, and Bagi [13] used this as a reference value for comparison. However, when element tests of granular materials are conducted, the stress–strain behaviour of large masses of soil is needed, and it is therefore the strain remote from the boundary that is required. As can be seen in Figure 3, the best-fit strain was more representative of the strain in the region far from the boundaries, leading to the conclusion that the best-fit strain is a better measure of the far-field behaviour of a granular material. It should therefore be calculated whenever possible (e.g. in DEM simulations) as it automatically excludes the boundary effect. Nevertheless, this is not routinely done.

The reason why the best-fit strain works better is that the boundary region only contains a small proportion of the total number of particles, and any non-representative strain values influence the calculation only slightly. The best-fit value will be the one that fits the strain value for the majority of the grains, with the non-representative strains for the few particles in the region affected by the boundary influencing the calculation only slightly. On the other hand, the macro strain (calculated from boundary displacements) is a volume average strain and hence is equal to the mean value of the individual local strains. Any discrepancies between these two strain measures should be attributed to the relatively large values for strain within the small boundary regions. Having established that the best-fit strain is a better measure of bulk material deformation, it was included in the plot of vertical stress versus vertical strain in Figure 6.

Figure 6 shows that the use of macro strain leads to an initial large underestimation of the far-field material stiffness. The underestimation of small-strain stiffness is a well-known problem arising in laboratory tests but not much discussed in DEM simulations. This should be attributed solely to the unrepresentative large strain of the voids at the interface between a rigid boundary and a non-conforming granular surface. One can observe in Figure 6 that the discrepancy between

DOI: 10.1002/nag

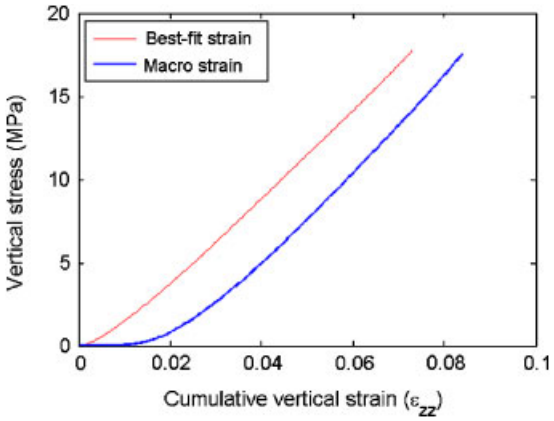

Figure 6. Vertical stress versus cumulative macro and cumulative best-fit vertical strain.

Table I. The components of the best-fit strain tensors and the boundary macro strain for the increment from 0 to 1 MPa (compression is positive and strains are given in %).

	ε_{xx}	ε_{yy}	ε_{zz}	ε_{xy}	ε_{xz}	ε_{yz}
Whole sample (best-fit)	−0.15	−0.10	0.72	0.02	−0.02	−0.05
1st slice from bottom	−0.24	−0.08	7.31	0.02	0.93	−0.02
2nd slice from bottom	−0.13	0.00	2.41	0.03	−0.01	0.11
A middle slice	−0.03	−0.04	0.82	0.00	0.06	−0.19
3rd slice from top	−0.57	−0.34	0.91	0.03	−0.58	0.04
2nd slice from top	−0.61	−0.20	−10.14	0.17	−0.70	0.58
1st slice from top	−0.68	−0.22	94.17	0.19	6.48	−2.72
Macro strain	0	0	2.13	0	0	0

the two strain values peaked at a stress of 5.1 MPa, and then slightly decreased as the boundary layers stiffened.

The presence of the boundary had largest relative effects, producing non-representative strain values, during the initial part of the stressing. Further discussion will focus on this initial stage of stressing. The values of the other components of the local strain tensor (ε_{xx}, ε_{yy}, ε_{zz}, ε_{xy}, ε_{xz}, ε_{yz}) for a number of horizontal slices are shown in Table I for the stress increment from 0 to 1 MPa. One should note that as the strain tensor is symmetric $\varepsilon_{ij} = \varepsilon_{ji}$.

When looking at the strain components in all other directions, the total macro strain based on boundary displacements was zero (1D compression) while the best-fit strain value was -0.10% for ε_{xx} and -0.15% for ε_{yy} between 0 and 1 MPa (see Table I). This indicated that the particles expanded into the voids at the vertical grain-boundary interface and slight lateral expansion was observed for the other strain increments also. One should however note that the overall ratio of best-fit strain components $\varepsilon_{xx}/\varepsilon_{zz}$ or $\varepsilon_{yy}/\varepsilon_{zz}$ diminished as the stressing progressed. Furthermore, the value of these lateral strains would be roughly proportional to the ratio of particle diameter to sample width. This is because the lateral strains arose from the deformation of the boundary voids whose volume would be independent of specimen size due to the fact that they are caused

DOI: 10.1002/nag

by a lack of fit between a flat surface and spherical grains. These observations are particularly relevant to sand testing using an oedometer, and demonstrate that what would be perceived as 1D compression might in fact not be so, as the lateral strain values might not always be negligible. One should note here that the more representative best-fit lateral strain values were approximately 20% of the best-fit axial strain values up to 1 MPa.

The values of best-fit shear strains on the faces of the whole sample were very close to zero as expected for all stress increments. Even though the observed overall shearing of the sample was negligible, the local shear strains in the slices near the top boundary were not (Table I), indicating a region of particle mixing/dilation at the top boundary that was separately confirmed to extend up to five mean grain diameters from it.

PARTICLE DISPLACEMENT FIELD

A projection of the particle displacement field for the increment between 0 and 1 MPa was plotted in Figure 7. For this plot a vertical plane containing the centroid of the topmost particle and parallel to one of the vertical walls was identified. The displacements of all particles intersecting the plane were plotted as 2D vectors on the plane at the projections of their centroids. This plotting procedure converted the difficult-to-visualize 3D data to a 2D data set. In doing so only a small proportion of the total number of vectors were plotted and the third component (perpendicular to the plane) of the displacement vector was lost. However, due to symmetry this third component did not differ from the one plotted, while similar behaviour was observed on other planes.

One should note that the top and bottom boundaries were moved by the same amount inwards when the simulation was performed (1.14 mm). Despite this, the particle displacement field was not symmetric about the middle of the sample, highlighting the different conditions at the top and bottom boundaries. Initially there were a large number of particles in contact with the bottom

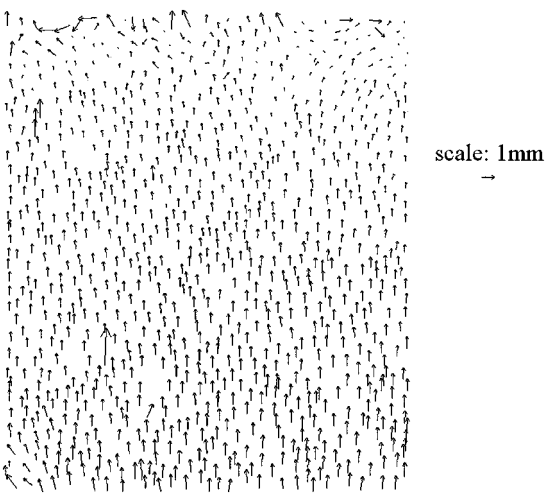

Figure 7. Displacement field on a vertical plane through the sample; stress increment 0–1 MPa. Only displacements for particles intersected by the plane are plotted.

DOI: 10.1002/nag

surface as the particles were sequentially deposited on it ('best-case contact'). At the top, on the other hand, there were far fewer particle-boundary contacts and a much larger void volume ('worst-case contact'). On stressing the sample, it was the large top void volume that was removed first, with most strain occurring there.

Figure 7 shows that the deformation at the top of the sample resembled a number of sand penetration tests at the sites of each salient contact. The process of forcing the topmost particles into the bulk of the sample is influenced by boundary velocity, in that local accelerations will be larger than those just beneath the loose zone. Since the speed of sample shortening to produce Figure 6 was quite large at 0.1 m/s, a study was also made of the effect of reducing this to 0.025 m/s and to 0.006 m/s. Rate effects were found only to influence the initial stages of the deformation of the sample and not the fundamental micro-mechanisms, nor the subsequent quasi-static stiffness response. The investigation of these rate effects on the initial stage of bedding deformation could be important in comparing slow triaxial test data with fast soil-wheel response, for example, but a deeper analysis falls beyond the scope of this work.

As seen in Table I the vertical strain for the topmost slice was extremely large (94%), which could be attributed to the relatively unresisted downward movement of the topmost particles. Particles one slice below this were pushed sideways by the ones above, inducing shear and dilation to fill the large void volume beneath the top boundary, see Figure 7. This led to the overall *extension* observed in the second slice, as documented by the tensile ε_{zz} strain in Table I. Strain values in the slices below this progressively returned to normal levels. However as any DEM sample is inhomogeneous at the particle level, even the middle slices deviated from the best-fit strain for the whole sample, as seen in Figure 3.

Close to the bottom boundary the particle movement pattern was very different. Here, local compression of boundary voids was again observed, but these voids were much smaller because of the sample preparation method. More particles were initially in contact ('best-case contact') with the bottom boundary and then followed its movement. Therefore, no dilatant/expanding region was observed, but rather a smooth drop to background strain values.

All of the above observations were echoed on Figure 3. A fairly constant level of vertical straining for the central region can be identified, being the strain value most representative of the sand's behaviour as a whole. There is a small region within about two mean particle diameters of both top and bottom boundaries where the strain values deviated significantly from this value, leading to problems when boundary displacement values were used for strain calculation, as discussed above.

A plot after the fashion of Figure 7 is shown in Figure 8 for the stress increment 1–6 MPa; a similar picture emerged for 6–12 MPa. One can note here that the particle displacements became more symmetric about the middle of the sample, indicating that the effect of the preparation method had significantly reduced, with the majority of the top boundary voids removed. However, some boundary effects remained, as indicated by the difference between the boundary and best-fit strains (see Figure 4). One should recall that these plots are for a sample with a ratio of maximum to minimum grain size of 2. The micromechanisms of grain deformations presented in Figures 7 and 8 should nevertheless provide invaluable insight into local grain movements for samples with wider grain size distributions too, as these are mostly controlled by the lack of fit between the curved grains and a flat surface. In addition, the concepts of a 'best-case' and 'worst-case' contact would still be applicable, providing a powerful framework for rationalizing boundary effects.

Having investigated the inhomogeneities in the strain field it is now interesting to see to what extent the particle structure and force network has been affected by stressing inside the cell bounded

DOI: 10.1002/nag

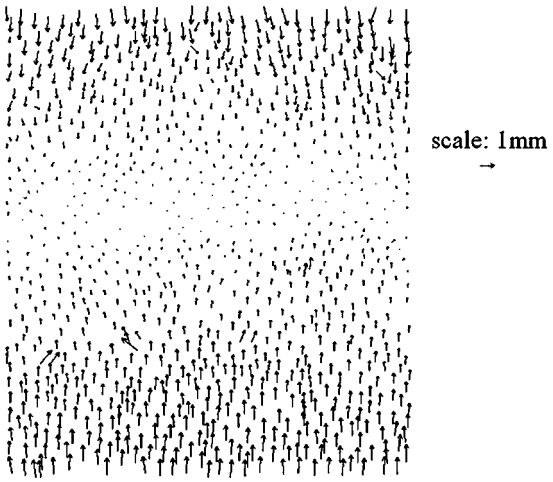

Figure 8. Displacement field on a vertical plane through the sample; stress increment 1–6 MPa. Only displacements for particles intersected by the plane are plotted.

by flat boundaries. The sample at 6 MPa was inspected and the relevant data obtained. The simplest measure of particle structure is the porosity of the particle packing, and this will be presented first.

THE EFFECT OF THE BOUNDARY ON POROSITY

At 6 MPa the simulation was paused and the sample volume was divided into slices which extended throughout the whole sample in the horizontal direction, but this time had a thickness of 0.2 mean particle diameters (i.e. 0.6 mm). This high-resolution local porosity data were subjected to a 10-point moving average filter. Ten adjacent slices were grouped together and the mean porosity is plotted against the mean position above the bottom boundary in Figure 9. Lines marking the mean porosity and the upper and lower 1% probability limits are also included. These were calculated from data for the middle $\frac{3}{8}$ths of the sample, a region that was assumed to be unaffected by the presence of the top or bottom platens.

In Figure 9 one can easily identify a boundary region where the porosity (void density) was high, a region where the porosity was minimum and the solid density peaked due to the orderly packing of spheres and a middle region where there were random fluctuations in porosity that can be associated with random fluctuations in the non-crystal packing of the grains. One can further note that the top and bottom boundary slices differed slightly in porosity. As noted earlier, the sample preparation technique allowed the bottom particles to pack closely to the bottom boundary, whereas the top boundary was placed after the sample was created.

Coherent data lying outside the middle 98% probability region bounded by the 1-in-100 probability lines indicate the presence of a non-random factor affecting porosity. In this way, the boundary region width was estimated as 2 mean diameters for the lower boundary region, and 6 diameters for the top (see Figure 9). This establishes that the relatively poor contact conditions at the top boundary resulting from the sample preparation method created a zone of local rearrangement

DOI: 10.1002/nag

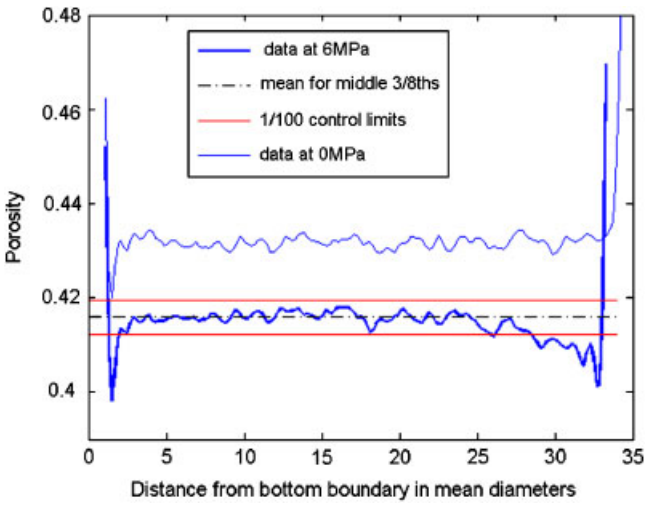

Figure 9. The mean porosity for 10 horizontal slices versus height above the bottom boundary at 6 MPa. The data for the sample at its unstressed state are shown too.

about 6 particle diameters deep. The small shear strain cycle occurring between roughly 2 and 6 diameters from the top boundary resulted in additional compaction, creating a slightly higher solid density. A porosity variation of 2–3% relative to the mean is observed between 2 and 6 diameters separation, extending further than what was previously thought to be [3–5]. Notwithstanding this zone of slight compaction, the layer immediately adjacent to the top boundary remained of lower grain density (higher porosity), which will be found to affect the number of points of force transmission between the boundary and the sample.

Figure 9 also plots the data for porosity for the sample at its unstressed state, similar to the data at 6MPa. As no straining has occurred, the mean of the local porosity values are higher. One should note that the drop at a distance of approximately 1.5 mean grain diameters from the bottom boundary is observed here too, as this is due to the sample preparation method. However, at the top the picture is different with no drop in the porosity observed, as straining has not occurred and the grain packing has not rearranged yet so as to ensure good contact between the grains and the flat surface. One should note that comparison between the two porosity profiles can explain the local strain variations observed between 0 and 6 MPa.

One should also note that the 1% probability threshold was chosen empirically on the basis that no data for the middle of the sample fell outside. A higher probability threshold would slightly increase the value quoted for the extent of the boundary region but would also create spurious anomalies in the central region.

THE EFFECT OF THE BOUNDARY ON THE STRONG FORCE NETWORK

In many cases one might argue that it is not the grain density/porosity that is important, but rather that the strong force network (see [15]) and its 3D structure is what governs the observed behaviour. For example, the largest forces will be responsible for crushing or cracking of grains,

DOI: 10.1002/nag

and their positions inside a sample will govern the locations of grain failure. One should therefore attempt to quantify any difference in the strong force network that is induced near a boundary. However, there is a wealth of information associated with such a 3D network, making its concise description difficult.

In the approach proposed here, the maximum normal contact force acting on a particle was considered to be a good descriptor for the local force distribution around it. Its value was assigned at the centre of each particle and a threshold of force was then set, above which all forces were considered as significant. The sample was then divided as before in horizontal slices and the number of particles having a maximum normal contact force exceeding the threshold value was calculated for each slice, while two different threshold values were implemented.

The number of particles carrying normal contact forces larger than Fmean (the mean maximum particle normal contact force) and 2 Fmean, plotted versus distance from the bottom boundary, are shown in Figures 10(a) and (b), respectively. One should note again that the data of 10 thin slices were grouped to reduce randomness and enable identification of any trend. For Figure 10(a) the force threshold was too low, and the inherent randomness masked the boundary effect. However, the more extreme incidences recorded in Figure 10(b) clearly display the significant influence of the top and bottom boundaries. Furthermore, the plot discriminates between their relative effects, with a smaller number of extreme incidences ($F>2$ Fmean) at the bottom boundary, where the particles were deposited sequentially on a smooth surface, and a larger number at the top boundary, where particles whose tops were sticking out were preferentially stressed. Figure 11 highlights this effect. Here, only the contacts between grains and the top or bottom boundaries were considered, and the number of particle contact forces lying in a specific range was plotted versus the normal contact force. One should note that there were 591 particles in contact with the bottom wall, and 475 with the top (20% less), but the incidence of extreme values was more striking, with 23 contacts carrying $F>4$ Fmean at the top boundary and none at the bottom.

This difference was echoed in the distance required for the far-field pattern of the force network to be attained. Forces branch off and converge on particles in every layer. A greater distance is required for a large number of extreme forces to dissipate into the far-field force network. That

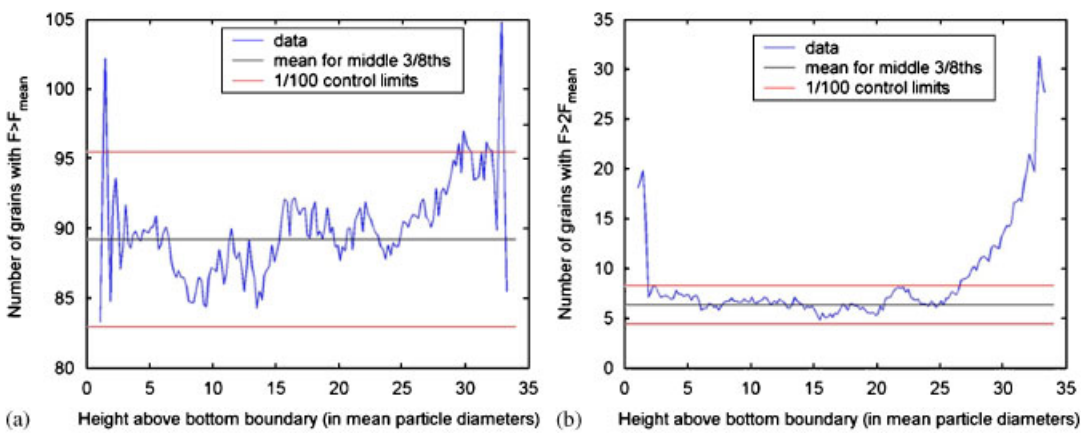

Figure 10. Plots at 6 MPa of the number of particles carrying normal contact forces larger than (a) Fmean and (b) 2 Fmean versus distance from the bottom boundary.

DOI: 10.1002/nag

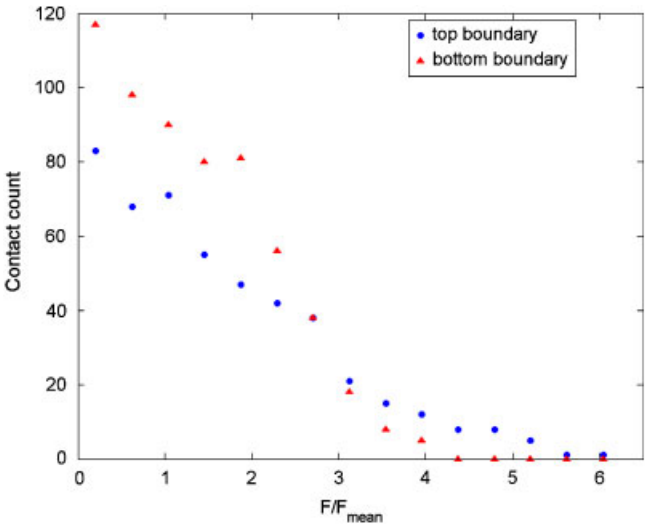

Figure 11. Count of grain-wall contacts with forces lying in a specific force magnitude range versus non-dimensionalized normal contact force, for the sample at 6 MPa.

is why Figure 10(b) showed the boundary region extending only over 2 particle diameters at the bottom of the specimen in comparison to 8 diameters at the top. One should note that a subsequent study into the effects of the boundary velocity [10] has indicated that a lower velocity (6.25 mm/s) would somewhat reduce the observed width of the region with a perturbed strong-force network to 6 mean grain diameters. This rate effect will not be expanded on here.

CONCLUSIONS

This study has shown that the strain quantity most representative of the behaviour of large masses of granular materials, free from any boundary effects, is the best-fit strain calculated by making use of individual particle displacements. This strain calculation method should be the one used in DEM simulations, and might also be applicable in physical tests if CT scanning provides sufficient resolution of particle displacements. The volume-average strain calculated in the classical way from boundary displacements can give non-representative results, here overestimating the best-fit strain by a factor of 3 for the stress interval between 0 and 1 MPa. This corresponds with the acknowledged underestimation of the small-strain stiffness of soils when laboratory tests depend on platen displacements instead of using internal strain measurement.

The discrepancy in the strain values is due to the compression of unrepresentatively large voids adjacent to the grain-boundary interface, especially where a solid surface has been placed on top of a pre-formed granular layer. If strain values representative of the interior of the soil are required, such boundary effects must be circumvented. In DEM, one way of avoiding such problems is to use periodic boundaries (e.g. [16]). The current work has shown that another solution is to employ best-fit strains. In laboratory element tests, where individual particle displacements are no longer

DOI: 10.1002/nag

available, the only way of avoiding bedding and boundary errors is to define a gauge length using strain markers sufficiently far from the boundaries (e.g. [1]). This study has shown that the local strain field inside a sample suffering 1D compression varied significantly from the representative interior value in a region extending about 2 mean particle diameters from each rigid boundary.

The current study has highlighted that pluviated granular materials form two distinctly different types of contact with a flat object such as a boundary. In the study here, the bottom boundary region contained a 'best-case' sand-boundary interface with a large number of grains in contact with it. The top boundary region contained a 'worst-case' interface with a larger number of voids and less grain-boundary contacts. Such boundary regions can also be identified in a number of other engineering applications (see Figure 1).

When porosity differences were considered, the boundary effect was found to extend 2 mean particle diameters from a smooth, solid boundary over which the granular material had been placed, for a sand with a ratio of maximum to minimum grain size of 2. In the case of a plane boundary placed on top of a pre-existing granular layer, however, the modified porosity zone was found to extend as far as 6 mean particle diameters. A boundary region with a different porosity would also show different transport properties. The high porosity adjacent to the sand-boundary interface creates a preferential flow path, as shown by Sentenac *et al.* [17].

When the contact force distribution inside the sample was inspected, a variation in the number of extreme forces could be detected to a much larger distance. For the zone adjacent to the top boundary, the frequency of occurrence of forces larger than 2 Fmean was double that of the representative mid-sample value even at a boundary separation of five particles, while a difference was detected up to 8 diameters away, much larger than what might have been presumed. Particle crushing and fracture are therefore much more likely to initiate in the boundary region; this has been reported for DEM simulations [18]. Experiments on sand, even at moderate stress levels, should be carefully designed in order to ensure that the observed behaviour is not obscured by preferential grain crushing at the boundary.

The large extent of the disturbed boundary region reported here suggests that previous recommendations for the ratio of sample size to maximum particle size in laboratory testing are too low, especially where grain damage may be significant. For example, Head [2] suggests minimum ratios of 5, 6, 10 or 12, depending on the nature of the laboratory test. In general, one should ensure that the boundary region is much smaller than the sample so as to minimize its effect on the test to be performed. However, Head's recommendations might result in the entire sample falling within the influence zone of one or other boundary.

One should note that the results presented here are for a granular sample with a ratio of maximum to minimum grain size of 2, which is the same as that often used in laboratory tests (e.g. when testing sands of Fractions A to E). One would expect the extent of the boundary region to be dependent on the width of the grain size distribution. Nevertheless, it should in principle be possible to express this as a function of a single descriptor of the grain size distribution. We have chosen this to be the mean grain size here, but other quantities such as d_{10}, d_{25}, or d_{90} (for example) could be more important, and this remains a very important open question that should be addressed by further simulations.

The work also places an important qualification on the feasibility of modelling soil–structure interaction problems using a discrete element approach, especially if crushable particles were to be used in order to capture realistic plastic compression behaviour (as in [11]). A large smooth boundary, such as a foundation, would require the use of a large number of small particles in contact, to ensure that the boundary zone remains small in relation to the geometry of the boundary value

DOI: 10.1002/nag

problem. This may offer a practical constraint due to large computational times, until computer speed significantly increases.

ACKNOWLEDGEMENTS

The first author would like to thank the A. S. Onassis and the A. G. Leventis Foundations for their generous financial support. This work was carried out at the Cambridge University Engineering Department.

REFERENCES

1. Jardine RJ, Symes MJ, Burland JB. Measurement of soil stiffness in the triaxial apparatus. *Geotechnique* 1984; **34**(3):323–340.
2. Head KH. *Manual of Soil Laboratory Testing. Vol. 2*: *Compressibility, Shear Strength and Permeability* (2nd edn). Pentech Press: London, 1994.
3. Hardin BO. Effect of rigid boundaries on measurement of particle concentration. *Geotechnical Testing Journal* 1989; **12**(2):143–149.
4. Roblee LSH, Baird RM, Tierney JW. Radial porosity variations in packed beds. *AIChE Journal* 1958; **4**(4): 460–464.
5. Reyes SC, Iglesia E. Monte Carlo simulations of structural properties of packed beds. *Chemical Engineering Science* 1991; **46**(4):1089–1099.
6. Chan SK, Ng KM. Geometrical characteristics of a computer-generated three-dimensional packed column of equal and unequal sized spheres—with special reference to wall effects. *Chemical Engineering Communications* 1986; **48**(4):215–236.
7. Goodling JS, Khader MS. Co-ordination number distribution of spherical particles in a packed cylindrical bed. *Powder Technology* 1985; **44**:53–55.
8. Cundall PA, Strack ODL. A discrete numerical model for granular assemblies. *Geotechnique* 1979; **29**(1):47–65.
9. Itasca Consulting Group Inc. *PFC^{3D}*: *Particle Flow Code in 3 Dimensions*, *Version 3.0*, Minneapolis, 2003.
10. Marketos G. An investigation of crushing and compaction bands in granular material. *Ph.D. Thesis*, Cambridge University, U.K., 2007.
11. Cheng YP, Nakata Y, Bolton MD. Discrete element simulation of crushable soil. *Geotechnique* 2003; **53**(7): 633–641.
12. O'Sullivan C, Bray JD, Li S. A new approach for calculating strain for particulate media. *International Journal for Numerical and Analytical Methods in Geomechanics* 2003; **27**:859–877.
13. Bagi K. Analysis of microstructural strain tensors for granular assemblies. *International Journal of Solids and Structures* 2006; **43**(10):3166–3184.
14. Kuhn M. Structured deformation in granular materials. *Mechanics of Materials* 1999; **31**:407–429.
15. Radjai F, Wolf DE, Jean F, Moreau J-J. Bimodal character of stress transmission in granular packings. *Physical Review Letters* 1998; **80**(1):61–64.
16. Sitharam TG, Dinesh SV, Shimizu N. Micromechanical modelling of monotonic drained and undrained shear behaviour of granular media using three-dimensional DEM. *International Journal for Numerical and Analytical Methods in Geomechanics* 2002; **26**(12):1167–1189.
17. Sentenac P, Lynch RJ, Bolton MD. Measurement of the side-wall boundary effect in soil columns using fibre-optics sensing. *International Journal of Physical Modelling in Geotechnics* 2001; **1**(4):35–41.
18. Marketos G, Bolton MD. Compaction bands as observed in DEM simulations. *Proceedings of the 5th International Conference on Micromechanics of Granular Media*, *Powders and Grains*, Stuttgart, vol. 2, 2005; 1405–1409.

DOI: 10.1002/nag